ISSN 1330-3651 (Print), ISSN 1848-6339 (Online)
Received: 17 December 2025; Accepted: 26 March 2026

https://doi.org/10.17559/TV-20260305003437
Original scientific paper

Influence Analysis of Machining Taper on Force of Piston

Bin ZHANG, Shusheng LI*, Wenke GAO

Abstract: The piston-cylinder pair is one of the three key tribological interfaces in an axial piston pump. Machining taper and operational tilt jointly modify the oil-film thickness and, therefore, the pressure distribution, resultant hydraulic force, centre of pressure and viscous friction acting on the piston. In this study, an analytical model is established for the annular clearance while accounting for both piston tilt and machining taper. The effect of taper direction is then discussed through a case study of a CCY14-1B pump. The results show that taper direction has only a limited influence on the resultant hydraulic force, but it has a pronounced influence on viscous friction in both the suction and discharge zones. For the present case, the centre of pressure in the discharge zone is located close to the lower one-third of the sealing length measured from the piston bottom. The results should be interpreted as case-specific analytical/numerical predictions for the selected geometry and operating condition.

Keywords: axial piston pump; hydraulic force; machining taper; oil-film friction; piston posture

1 INTRODUCTION

Axial piston pumps are widely used in aerospace, construction machinery and other demanding hydraulic systems because of their high power density, compact structure and good controllability. Recent studies on accelerated life testing, pressure-pulsation optimisation, high-speed aircraft pumps and wear of the main moving pairs all show that reliability and tribological performance remain central engineering concerns [1-4].

Among the three principal friction pairs in an axial piston pump, the piston-cylinder interface directly influences leakage, load support, frictional loss and wear. Chen et al. analysed leakage while considering piston pose and machining taper [5], and Zheng et al. investigated the lubrication characteristics of the piston pair in a large-displacement axial piston pump [6]. A more complete treatment of leakage and output-flow ripple was reported in Ref. [7], while CFD was used in Ref. [8] to study the effect of piston grooves on pump performance. Additional studies have examined leakage under wear or remanufacturing conditions [9, 10] and the effect of elastic deformation on lubrication and leakage [11].

The literature also shows that piston micro-motion and cavity-pressure evolution have a strong influence on interface behaviour. Wang's thesis and related conference paper discussed piston-cylinder micro-motion and piston-cavity pressure in axial piston pumps [12, 13]. Oil-film characteristics of the piston-cylinder pair under ultra-high pressure were studied in Ref. [14], and a recent review summarised tribological characteristics and surface-texturing approaches for piston pairs [15]. The influence of fluid viscosity on lubrication behaviour has also been discussed in Ref. [16], whereas Ref. [17] analysed piston posture and interface leakage under changing rotational speed.

More recent international studies have pushed the topic towards tapered micro-geometry, tolerance design and coupled multi-physics analysis. Liu et al. investigated tapered-shape surface design of the piston bore [18], Wang et al. proposed a tolerance-design guideline based on a thermal-fluid-structure model [19], and Zhou et al. studied fluid-structure-thermal interaction in the piston-cylinder interface [20]. Hong and Shin further developed lubrication modelling for a reciprocating piston under high lateral load and various operating conditions [21]. In addition, simulation and experimental investigation of low-wear surface contours [22] and a broad review of structural improvement, material selection and surface treatment for axial-piston-pump friction pairs [23] both highlight the practical value of geometry-oriented design guidance.

These studies clearly demonstrate the importance of geometry, tilt, speed, viscosity, clearance and thermal effects. However, for engineering interpretation and rapid case evaluation, it remains useful to have a compact analytical description that isolates how machining taper direction interacts with piston tilt to modify the pressure distribution, resultant hydraulic force, centre-of-pressure location and viscous friction in the annular clearance.

Table 1 Nomenclature

Symbol	Meaning
x	Axial coordinate along the piston bore / flow direction
y, z	Lateral coordinates in the bore cross-section; z is the wall-normal direction in the local oil-film model
h	Local oil-film thickness
p, p_1, p_2	Gauge pressure and inlet/outlet pressures
t_0	Machining taper (positive or negative)
$e(x)$	Resultant eccentricity at axial position x
δ, δ_2, δ_m	Inlet, outlet and mean radial clearances
μ	Dynamic viscosity of the oil
u	Piston sliding velocity
FN, η	Oil-film normal load and normalised friction coefficient

Compared with Ref. [5], the present work does not focus only on leakage of a pose-and-taper model; instead, it extends the analysis to the resultant hydraulic force, the centre of pressure and the viscous-friction response of a tapered and tilted piston pair. Compared with Refs. [18-21], which emphasise tapered bore design, tolerance optimisation, multi-physics coupling and broader lubrication modelling, the present paper is deliberately narrower and more analytical: it provides a tractable case-study model that explicitly compares positive and negative taper directions for one selected pump geometry and operating condition. The contribution claimed here is therefore limited to: (i) an analytical force-oriented treatment of a tapered and tilted piston pair, (ii) an explicit comparison of taper-direction effects on hydraulic force

and viscous friction, and (iii) a compact prediction of the centre-of-pressure position along the sealing length.

To avoid overstatement, the revised manuscript treats the results as case-specific analytical/numerical predictions for the selected CCY14-1B pump rather than universal laws. This framing is consistent with the current level of validation and is intended to provide a clearer basis for subsequent experimental and multi-parameter studies. The main symbols used in the mathematical model and their physical meanings are summarized in Tab. 1.

2 METHOD

2.1 Oil-Film Pressure Distribution in the Piston Pair

Consider a thin oil film of height h filled with hydraulic fluid and formed between two walls moving with a relative velocity u. In the local lubrication derivation used below, x denotes the axial flow direction and z denotes the wall-normal direction of the thin film. When the walls are parallel, h is constant; for non-parallel walls, h varies along x, as shown in Fig. 1. Because h is very small compared with the other geometric dimensions, the flow in the clearance is treated as steady laminar lubrication flow dominated by viscous effects.

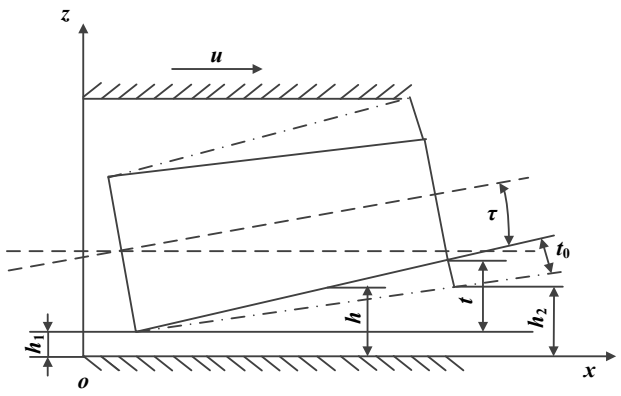

Figure 1 Schematic diagram of piston taper

Let the z-axis be perpendicular to the lower wall and the x-axis be aligned with the direction of flow. Under the lubrication approximation, $u_x = u$, $u_y = 0$, $u_z = 0$, and the body force acts only in the negative z-direction. This notation is used consistently in Eq. (1) to Eq. (11).

The continuity equation is given by:

$$\frac{\partial u_x}{\partial x}+\frac{\partial u_y}{\partial y}+\frac{\partial u_z}{\partial z}=0 \tag{1}$$

where u_x denotes the fluid velocity component along the x-axis; u_y denotes the fluid velocity component along the y-axis; and u_z denotes the fluid velocity component along the z-axis.

Based on these assumptions, the Navier-Stokes equations reduce to the lubrication form shown in Eq. (2).

$$\begin{cases} \dfrac{\partial u_x}{\partial x}=0 \\ 0=-\dfrac{1}{\rho}\dfrac{\partial p}{\partial x}+\gamma\dfrac{\partial^2 u_x}{\partial z^2} \\ 0=-\dfrac{1}{\rho}\dfrac{\partial p}{\partial y} \\ 0=-g-\dfrac{1}{\rho}\dfrac{\partial p}{\partial z} \end{cases} \tag{2}$$

where p represents the fluid pressure within the annular clearance between the piston and the cylinder bore.

Integrating the fourth expression in Eq. (2) gives $p = -\rho g z + f(x)$. Because the film thickness is very small, the hydrostatic variation across z is neglected and p may be treated as a function of x only. Moreover, the dominant velocity gradient is in the wall-normal (z) direction, so derivatives along x and y are neglected relative to the z-gradient. Therefore, Eq. (3) follows.

$$\frac{\partial^2 u_x}{\partial z^2}=\frac{1}{\rho\gamma}\frac{\mathrm{d}p}{\mathrm{d}x}=\frac{1}{\mu}\frac{\mathrm{d}p}{\mathrm{d}x} \tag{3}$$

The velocity distribution is given by:

$$u_x=\frac{1}{2\mu}\frac{\mathrm{d}p}{\mathrm{d}x}z^2+c_1 z+c_2 \tag{4}$$

Assuming that the upper wall moves with velocity u while the lower wall remains stationary, the boundary conditions are defined as:

$$u_x\big|_{z=0}=0,\ u_x\big|_{z=h}=u \tag{5}$$

Applying the boundary conditions yields the velocity distribution within the annular clearance:

$$u_x=-\frac{1}{2\mu}\frac{\mathrm{d}p}{\mathrm{d}x}(h-z)z+u\frac{z}{h} \tag{6}$$

The pressure gradient along the x-axis is given by:

$$\frac{\mathrm{d}p}{\mathrm{d}x}=-\frac{12\mu}{h^3}\frac{\delta q}{\delta y}+\frac{6\mu u}{h^2} \tag{7}$$

where μ denotes the dynamic viscosity of the fluid.

Assuming a linear variation of the clearance, $h = h_1 + (x/l)\,t$, we have $\mathrm{d}x = (l/t)\,d\mathrm{h}$. Integrating $d\mathrm{p}/d\mathrm{x}$ subject to $p(x = 0) = p_1$ and $p(x = l) = p_2$ gives Eq. (8) to Eq. (10).

$$p=\frac{6\mu l}{t}\frac{\delta q}{\delta y}\left(\frac{1}{h^2}-\frac{1}{h_1^2}\right)-\frac{6\mu u l}{t}\left(\frac{1}{h}-\frac{1}{h_1}\right)+p_1 \tag{8}$$

Substituting $x = l$ yields:

$$p_2=\frac{6\mu l}{t}\frac{\delta q}{\delta y}\left(\frac{1}{h_2^2}-\frac{1}{h_1^2}\right)-\frac{6\mu u l}{t}\left(\frac{1}{h_2}-\frac{1}{h_1}\right)+p_1 \tag{9}$$

Rearranging Eq. (9) gives:

$$\frac{\delta q}{\delta y}=\frac{\left(p_2-p_1\right)h_1^2h_2^2t+6\mu ulh_1h_2\left(h_1-h_2\right)}{6\mu l\left(h_1^2-h_2^2\right)} \tag{10}$$

From Eq. (8) and Eq. (10), the oil film pressure distribution in the annular clearance of the piston pair is obtained as:

$$p=\frac{6\mu l}{t}\left(\frac{1}{h^2}-\frac{1}{h_1^2}\right)\cdot\frac{p_2-p_1+\frac{6\mu ul}{t}\left(\frac{1}{h_2}-\frac{1}{h_1}\right)}{\frac{6\mu l}{t}\left(\frac{1}{h_2^2}-\frac{1}{h_1^2}\right)}-$$
$$-\frac{6\mu ul}{t}\left(\frac{1}{h}-\frac{1}{h_1}\right)+p_1 \tag{11}$$

Fig. 2 illustrates the actual posture of the tilted piston. Let e_2 and e_4 denote the lateral offsets at the piston end adjacent to the valve plate, and let e_1 and e_3 denote the offsets at the distal end. A coordinate system fixed to the cylinder block is established at the piston end near the valve plate. The piston velocity u is taken as negative in the discharge zone and positive in the suction zone.

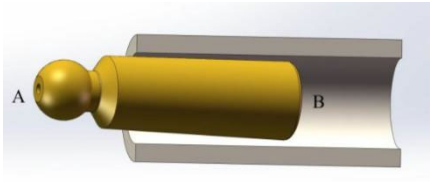

Figure 2 The true position of the piston

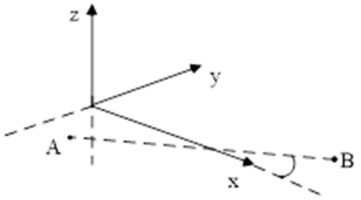

Figure 3 Piston coordinate system

The coordinates of the endpoints of the piston axis are A(0, e_2, e_4) and B(l, e_1, e_3), respectively. The axis equation is $x/l=(y-e_2)/(e_1-e_2)=(z-e_4)/(e_3-e_4)$, as shown in Fig. 3. Rearranging this relation yields Eq. (12).

$$\begin{cases} y=\dfrac{x\left(e_1-e_2\right)}{l}+e_2 \\ z=\dfrac{x\left(e_3-e_4\right)}{l}+e_4 \end{cases} \tag{12}$$

The direction vector of the cylinder bore axis is given by n = "(1, 0, 0)" . Consequently, the inclination angle τ of the piston axis relative to the cylinder bore axis satisfies:

$$\cos\tau=\frac{\left|\vec{n}\cdot\overrightarrow{AB}\right|}{|n|\cdot|AB|}=\frac{l}{\sqrt{l^2+\left(e_1-e_2\right)^2+\left(e_3-e_4\right)^2}} \tag{13}$$

$$\tau=\arccos\frac{l}{\sqrt{l^2+(e_1-e_2)^2+(e_3-e_4)^2}} \tag{14}$$

As shown in Fig. 4, because the inclination angle of the piston within the bore is small, the piston cross-section at axial position x is approximated as a circle. The coordinates of the centre of this circle are then obtained from Eq. (12).

$$C\left(x,\ \frac{x\left(e_1-e_2\right)}{l}+e_2,\ \frac{x\left(e_3-e_4\right)}{l}+e_4\right)$$

At position x, the resultant eccentricity can be expressed as:

$$e\left(x\right)=\sqrt{(\frac{x\left(e_1-e_2\right)}{l}+e_2)^2+(\frac{x\left(e_3-e_4\right)}{l}+e_4)^2} \tag{15}$$

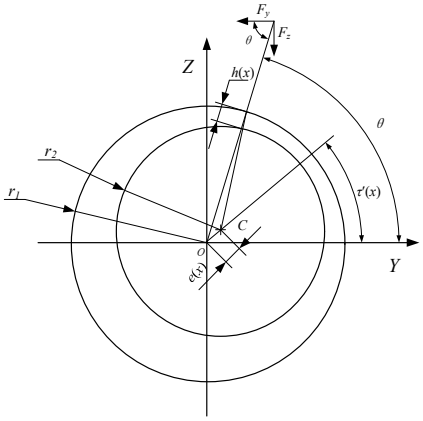

Figure 4 Piston hole coordinates

The eccentricity angle is given by:

$$\tau'\left(x\right)=\arctan\frac{\frac{x\left(e_3-e_4\right)}{l}+e_4}{\frac{x\left(e_1-e_2\right)}{l}+e_2} \tag{16}$$

Let $a=\frac{e_1-e_2}{l}$ and $b=\frac{e_3-e_4}{l}$. Then, the resultant eccentricity and the eccentricity angle can be expressed in the following forms:

$$e\left(x\right)=\sqrt{\left(ax+e_2\right)^2+\left(bx+e_4\right)^2} \tag{17}$$

$$\tau'\left(x\right)=\arctan\frac{bx+e_4}{ax+e_2} \tag{18}$$

Let r2 and r1 denote the piston radius and the cylinder-bore radius, respectively, at the piston end adjacent to the valve plate. Taking the inlet geometry as the reference, the radial clearance is $\delta = r_1 - r_2$. The circumferential film thickness at axial position x is then expressed by Eq. (19).

$$\begin{aligned} h(x) &= r_1 - \left[r_2 + e(x)\cos\left(\theta - \tau'(x)\right)\right] \\ &= r_1 - r_2 - e(x)\cos\left(\theta - \tau'(x)\right) \\ &= \delta - e(x)\cos\left(\theta - \tau'(x)\right) \\ &= \delta\left[1 - \frac{e(x)}{\delta}\cos\left(\theta - \tau'(x)\right)\right] \end{aligned} \tag{19}$$

Let $\varepsilon = e/\delta$ denote the eccentricity ratio.

$$h(x) = \delta\left[1 - \varepsilon(x)\cos\left(\theta - \tau'(x)\right)\right] \tag{20}$$

At the inlet:

$$h_1 = h(0) = \delta\left[1 - \varepsilon(0)\cos\left(\theta - \tau'(0)\right)\right] \tag{21}$$

At the outlet:

$$h_2 = h(l) = \delta\left[1 - \varepsilon(l)\cos\left(\theta - \tau'(l)\right)\right] \tag{22}$$

Considering practical manufacturing errors, the piston taper is denoted by t_0, which may be positive or negative. Because the tilt angle is small, the taper modifies the local film thickness through the geometric relation used in Eq. (21) to Eq. (23).

$$\begin{aligned} t &= h_2 - h_1 + t_0 \\ h' &= h_1 + \frac{x}{l}t = h_1 + \frac{x}{l}\left(h_2 - h_1 + t_0\right) \end{aligned} \tag{23}$$

Therefore, when piston tilt and machining taper coexist, the oil-film pressure distribution is given by Eq. (24).

$$\begin{aligned} p = {} & \frac{6\mu l}{t}\left(\frac{1}{h'^2} - \frac{1}{h_1^2}\right)\cdot\frac{p_2 - p_1}{\dfrac{6\mu l}{t}\left(\dfrac{1}{h_2'^2} - \dfrac{1}{h_1^2}\right)} + \\ & + \frac{\dfrac{6\mu u l}{t}\left(\dfrac{1}{h_2'} - \dfrac{1}{h_1}\right)}{\dfrac{6\mu l}{t}\left(\dfrac{1}{h_2'^2} - \dfrac{1}{h_1^2}\right)} - \frac{6\mu u l}{t}\left(\frac{1}{h'} - \frac{1}{h_1}\right) + p_1 \end{aligned} \tag{24}$$

Here p_1 and p_2 denote the inlet and outlet gauge pressures, respectively.

$$h_2' = h_1 + t = h_2 + t_0$$

Let $h(x, \theta)$ denote the actual film thickness at axial position x and circumferential position θ, and let $h(l, \theta)$ denote the outlet film thickness. The pressure distribution is then written as Eq. (25). In this paper, all reported pressures are gauge pressures unless otherwise stated. Because no cavitation boundary or pressure floor is imposed in the present analytical model, any negative values in the suction zone should be interpreted as indicators of pressure-depletion tendency rather than as physically sustainable absolute pressures.

$$\begin{aligned} p = {} & \frac{\dfrac{6\mu l}{t}\left(\dfrac{1}{h'^2} - \dfrac{1}{h_1^2}\right)\cdot\left(p_2 - p_1\right) + \dfrac{6\mu u l}{t}\left(\dfrac{1}{h_2'} - \dfrac{1}{h_1}\right)}{\dfrac{6\mu l}{t}\left(\dfrac{1}{h_2'^2} - \dfrac{1}{h_1^2}\right)} - \\ & - \frac{6\mu u l}{t}\left(\frac{1}{h'} - \frac{1}{h_1}\right) + p_1 \end{aligned} \tag{25}$$

2.2 Hydraulic Force Acting on the Piston

Let dFp denote the elemental hydraulic force acting on a piston wall segment of axial length dx and arc length r dθ. The resultant surface integral of pressure over the wetted wall is termed the hydraulic force in this paper.

$$\delta F = \int_0^l p\delta y\mathrm{d}x = \int_0^l p\delta y\frac{l}{t}\mathrm{d}h' = \frac{l}{t}\delta y\int_0^l p\mathrm{d}h' \tag{26}$$

$$\begin{aligned} \frac{\delta F}{\delta y} &= \frac{l}{t}\int_0^l p\mathrm{d}h' \\ &= \frac{l}{t}\int_{h_1}^{h_2'} p_1 + \left(p_2 - p_1\right)\frac{h_2'^2\left(h_1^2 - h'^2\right)}{h'^2\left(h_1^2 - h_2'^2\right)} + \\ &+ \frac{6\mu u l}{t}\frac{\left(h_1 - h'\right)\left(h_2' - h'\right)}{h'^2\left(h_1 + h_2'\right)}\mathrm{d}h' \\ &= \frac{p_1 + p_2}{2}l + \left[\begin{array}{l} \dfrac{\left(p_2 - p_1\right)t}{2} \\ + \dfrac{12\mu u l}{t} \end{array}\right]\frac{l}{2h_1 + t} + \frac{6\mu l^2 u}{t^2}\ln\frac{h_1}{h_1 + t} \end{aligned} \tag{27}$$

Let the centre of pressure of the resultant hydraulic force be located at axial position xcp. By the theorem of moments, Eq. (28) is obtained.

$$\begin{aligned} \delta F\cdot X &= \int_0^l\left(p\delta y\right)\cdot x\mathrm{d}x = \delta y\int_0^l px\mathrm{d}x \\ &= -\delta y\frac{h_1 l}{t}\left[\begin{array}{l} p_1 l + \left(p_2 - p_1\right)l\dfrac{h_1 + t}{2h_1 + t} + \\ + \dfrac{6\mu l^2 u}{t^2}\left(\dfrac{2t}{2h_1 + t} + \ln\dfrac{h_1}{h_1 + t}\right) \end{array}\right] + \\ &+ \delta y\frac{l^2}{t^2}\left[\begin{array}{l} \dfrac{p_1 t\left(2h_1 + t\right)}{2} + \\ + \left(p_2 - p_1\right)\dfrac{h_1^2\left(h_1 + t\right)^2}{\left(2h_1 + t\right)t}\ln\dfrac{h_1}{h_1 + t} + \\ + \dfrac{\left(p_2 - p_1\right)\left(h_1 + t\right)^2}{2} - \\ - \dfrac{6\mu l u}{t}\left(\dfrac{h_1\left(h_1 + t\right)}{2h_1 + t}\ln\dfrac{h_1}{h_1 + t} + \dfrac{3t}{2}\right) \end{array}\right] \end{aligned} \tag{28}$$

The centre-of-pressure location xcp is obtained from Eq. (29).

$$X = \frac{\frac{l^2}{t^2}\left[\frac{p_1 t(2h_1+t)}{2}+(p_2-p_1)\frac{h_1^2(h_1+t)^2}{(2h_1+t)t}\ln\frac{h_1}{h_1+t}\right]}{p_1 l+(p_2-p_1)l\frac{h_1+t}{2h_1+t}+\frac{6\mu l^2 u}{t^2}\left(\frac{2t}{2h_1+t}+\ln\frac{h_1}{h_1+t}\right)} + \frac{\frac{(p_2-p_1)(h_1+t)^2}{2}}{p_1 l+(p_2-p_1)l\frac{h_1+t}{2h_1+t}+\frac{6\mu l^2 u}{t^2}\left(\frac{2t}{2h_1+t}+\ln\frac{h_1}{h_1+t}\right)} \frac{\frac{(p_2-p_1)(h_1+t)^2}{2}-\frac{6\mu l u}{t}\left(\frac{h_1(h_1+t)}{2h_1+t}ln\frac{h_1}{h_1+t}+\frac{t}{2}\right)\Bigg]}{p_1 l+(p_2-p_1)l\frac{h_1+t}{2h_1+t}+\frac{6\mu l^2 u}{t^2}\left(\frac{2t}{2h_1+t}+\ln\frac{h_1}{h_1+t}\right)} - \frac{h_1 l}{t} \tag{29}$$

In the discharge zone, the centre of pressure is found to lie close to the piston end adjacent to the valve plate. Integrating the pressure over the circumference yields the resultant lateral force carried by the oil film.

$$F=\int_A \frac{\delta F}{\delta y}\mathrm{d}y,\ F=\int_A \frac{\delta F}{\delta y}\mathrm{d}y \tag{30}$$

The projections of the lateral force along the *y*- and *z*-axes are given by:

$$F_y=\frac{D}{2}\int_0^{2\pi}\frac{\delta F}{\delta y}\cos\theta\mathrm{d}\theta,\ F_z=\frac{D}{2}\int_0^{2\pi}\frac{\delta F}{\delta y}sin\,\theta\mathrm{d}\theta \tag{31}$$

The integrations lead to Eq. (32) and Eq. (33).

$$\begin{aligned}F_y=&\frac{Dl(p_2-p_1)}{4}\int_0^{2\pi}\frac{t}{2h_1+t}\cos\theta\mathrm{d}\theta\\&+6\mu uDl^2\int_0^{2\pi}\frac{1}{t(2h_1+t)}\cos\theta\mathrm{d}\theta\\&+3\mu uDl^2\int_0^{2\pi}\frac{1}{t^2}\ln\frac{h_1}{h_1+t}\cos\theta\mathrm{d}\theta\end{aligned} \tag{32}$$

$$\begin{aligned}F_z=&\frac{Dl(p_2-p_1)}{4}\int_0^{2\pi}\frac{t}{2h_1+t}\sin\theta\mathrm{d}\theta\\&+6\mu uDl^2\int_0^{2\pi}\frac{1}{t(2h_1+t)}\sin\theta\mathrm{d}\theta\\&+3\mu uDl^2\int_0^{2\pi}\frac{1}{t^2}\ln\frac{h_1}{h_1+t}\sin\theta\mathrm{d}\theta\end{aligned} \tag{33}$$

Because the integral is cumbersome, the resultant hydraulic force is evaluated by numerical quadrature of the analytical expressions.

$$F=\sqrt{F_y^2+F_z^2} \tag{34}$$

The angle between the resultant hydraulic force and the lateral reference direction is defined by Eq. (35).

$$\tan\theta_F=\frac{F_z}{F_y} \tag{35}$$

For the discharge zone, the centre of pressure is located near the piston end adjacent to the valve plate. For the suction zone, its axial location is obtained from Eq. (29) for each operating position.

2.3 Analysis of Piston Friction Force

The viscous friction acting on the piston surface is obtained by integrating the oil-film shear stress over the wetted area.

$$\begin{aligned}&\tau_\mu\big|_{z=h'}=\mu\frac{\partial u_x}{\partial z}\big|_{z=h'},\ t,\ \delta F_f=\int_A\tau_\mu\big|_{z=h'}\,\delta y\mathrm{d}x\\&\delta F_f=\delta y\int_0^l\tau_\mu\big|_{z=h'}\,\mathrm{d}x\end{aligned} \tag{36}$$

The velocity distribution used for the shear-stress evaluation is given above.

$$u_x=-\frac{1}{2\mu}(h'-z)z\frac{\mathrm{d}p}{\mathrm{d}x}+u\frac{z}{h'} \tag{37}$$

The corresponding viscous shear stress is expressed by Eq. (38).

$$\tau_\mu\big|_{z=h'}=\mu\frac{\partial u_x}{\partial z}\big|_{z=h'}=\frac{h'}{2}\frac{\mathrm{d}p}{\mathrm{d}x}+\frac{\mu u}{h'} \tag{38}$$

Using the velocity field above, the elemental friction force corresponding to arc length $r\,d\theta$ and axial length dx is given by Eq. (39) and Eq. (40).

$$\delta F_f=\int_A\tau_\mu|_{z=h'}\delta y\mathrm{d}x=\delta y\int_0^l\frac{h'}{2}\frac{\mathrm{d}p}{\mathrm{d}x}+\frac{\mu u}{h'}\mathrm{d}x \tag{39}$$

$$\begin{aligned}\frac{\delta F_f}{\delta y}&=\int_0^l\frac{h'}{2}\frac{\mathrm{d}p}{\mathrm{d}x}+\frac{\mu u}{h'}\mathrm{d}x\\&=-p_1\frac{h_1}{2}-\frac{t}{2l}\frac{\delta F}{\delta y}+\frac{\mu u l}{t}\ln\frac{h_1+t}{h_1}\end{aligned} \tag{40}$$

Integrating over the circumference yields the total friction force.

$$F_f = \int_0^{2\pi} \frac{\delta F_f}{\delta y} \mathrm{d}y = \frac{D}{2} \int_0^{2\pi} \frac{\delta F_f}{\delta y} \mathrm{d}\theta$$
$$\frac{\delta F_f}{\delta y} = \frac{p_1 + p_2}{2} l + \left[\frac{(p_2 - p_1)t}{2} + \frac{12\mu u l}{t} \right] \frac{l}{2h_1 + t} + \frac{6\mu l^2 u}{t^2} \ln \frac{h_1}{h_1 + t} \tag{41}$$

$$F_f = \frac{D}{2} \left[-\int_0^{2\pi} p_1 \frac{h_1}{2} \mathrm{d}\theta + \int_0^{2\pi} \frac{\mu u l}{t} \ln \frac{h_1 + t}{h_1} \mathrm{d}\theta - \frac{1}{2} \int_0^{2\pi} \frac{p_1 + p_2}{2} t + \pi \left[\frac{(p_2 - p_1)t}{2} + \frac{12\mu u l}{t} \right] \frac{t}{2h_1 + t} + \frac{6\mu l u}{t} \ln \frac{h_1}{h_1 + t} \mathrm{d}\theta \right] \tag{42}$$

Because the integral is cumbersome, the total friction force is evaluated numerically. In the present oil-film model, the normal load used to normalise friction is defined as $F_N = \sqrt{F_y^{\,2} + F_z^{\,2}}$, the magnitude of the resultant lateral supporting force carried by the oil film. Accordingly, $\eta = F_f/F_N$ is used here as a normalised friction indicator for comparing taper cases, rather than as direct proof of a dry or boundary-contact regime.

$$\eta = \frac{F_f}{F_N} \tag{43}$$

In the special case of zero taper and parallel axes, the piston becomes symmetric about the A-A axis and the simplified expressions for friction force and friction coefficient are given by Eq. (44) to Eq. (47).

$$F_f = \int_0^{2\pi} \frac{\delta F_f}{\delta y} \mathrm{d}y = \frac{D}{2} \int_0^{2\pi} \frac{\delta F_f}{\delta y} \mathrm{d}\theta = D \int_0^{\pi} \frac{\delta F_f}{\delta y} \mathrm{d}\theta \tag{44}$$

Substituting $\frac{\delta F_f}{\delta y}$ and integrating yields the friction force:

$$F_f = D \left[\frac{\pi p_2 (\delta + t_0)}{2} - \frac{\pi p_1 \delta}{2} - \frac{\pi (p_1 + p_2)}{4} t_0 \right] - \left[\frac{(p_2 - p_1)t_0}{4} + \frac{6\mu u l}{t_0} \right] t_0 \int_0^{\pi} \frac{1}{2\delta + t_0 - 2e\cos\theta} \mathrm{d}\theta - \frac{4\mu u l}{t_0} \int_0^{\pi} \ln \frac{\delta - e\cos\theta}{\delta + t_0 - e\cos\theta} \mathrm{d}\theta \tag{45}$$

By substitution, we obtain:

$$\int_0^{\pi} \frac{1}{2\delta + t_0 - 2e\cos\theta} \mathrm{d}\theta = \frac{\pi}{\sqrt{(2\delta + t_0)^2 - 4e^2}} \left(|2\delta + t_0| > |2e| \right)$$
$$\int_0^{\pi} \ln(\delta - e\cos\theta) \mathrm{d}\theta = \pi \ln \frac{\delta + \sqrt{\delta^2 - e^2}}{2} \tag{46}$$
$$\int_0^{\pi} \ln(\delta + t_0 - e\cos\theta) \mathrm{d}\theta = \pi \ln \frac{\delta + t_0 + \sqrt{(\delta + t_0)^2 - e^2}}{2}$$

$$F_f = \frac{\pi D (p_2 - p_1)}{4} \left[2\delta + t_0 - \frac{t_0^{\,2}}{\sqrt{(2\delta + t_0)^2 - 4e^2}} \right] - \frac{4\pi D \mu u l}{t_0} \left[\ln \frac{\delta + \sqrt{\delta^2 - e^2}}{\delta + t_0 + \sqrt{(\delta + t_0)^2 - e^2}} + \frac{3t_0}{2\sqrt{(2\delta + t_0)^2 - 4e^2}} \right] \tag{47}$$

Thus, the simplified friction coefficient for this special case is obtained.

3 RESULTS AND DISCUSSION

In this case study, a CCY14-1B axial piston pump is used as the reference geometry. The case-study parameters are listed in Tab. 2. Unless otherwise stated, the discharge and suction pressures are p_1 = 32 MPa and p_2 = 0 MPa (gauge), and the taper cases considered are t_0 = −2, −1, 0, 1 and 2 μm.

Table 2 Case-study parameters used in the numerical evaluation

Structural parameter	Value	Structural parameter	Value
Z	9	p_2 / MPa	0
γ / °	18	D / mm	18
R_f / mm	35	t_0 / μm	−2/−1/0/1/2
l_0 / mm	40	n / r·min^{-1}	1500
μ / Pa·s	8.7×10^{-3}	δ_m / μm	23
p_1 / MPa	32		

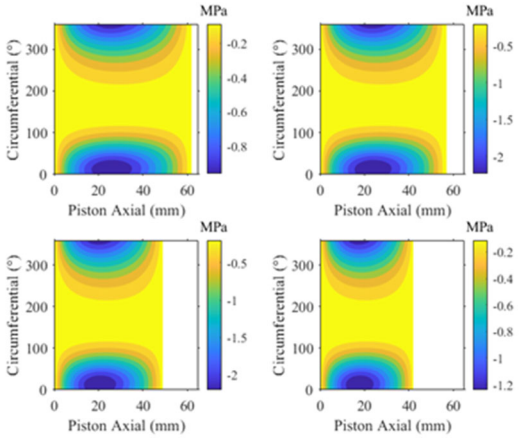

Figure 5 Pressure distribution in the low-pressure zone (t_0 = 2 μm)

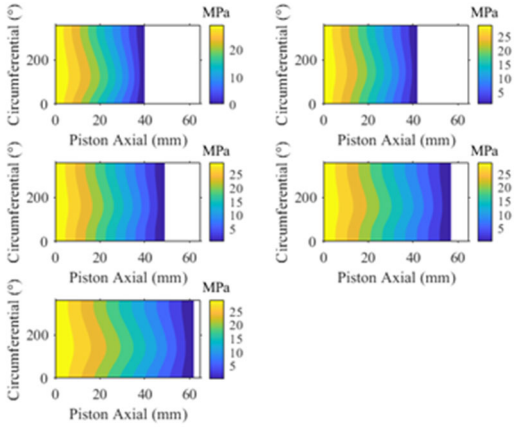

Figure 6 Pressure distribution in the high-pressure zone (t_0 = 2 μm)

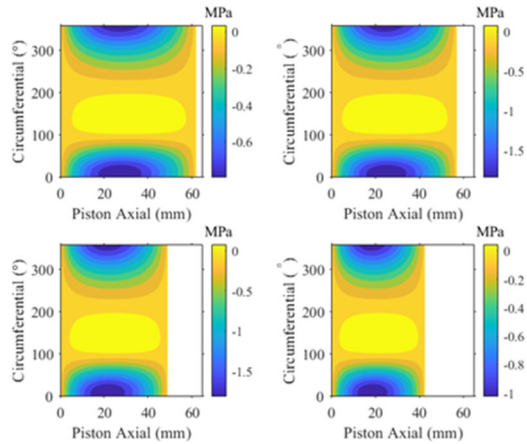

Figure 7 Pressure distribution in the low-pressure zone (t_0 = 1 μm)

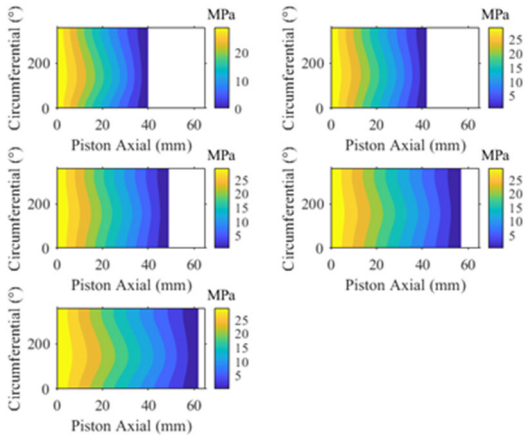

Figure 8 Pressure distribution in the high-pressure zone (t_0 = 1 μm)

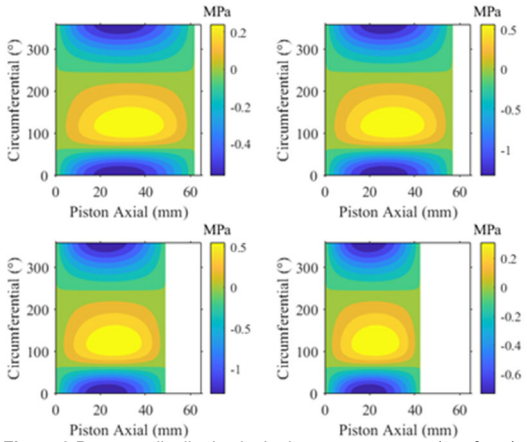

Figure 9 Pressure distribution in the low-pressure zone (t_0 = 0 μm)

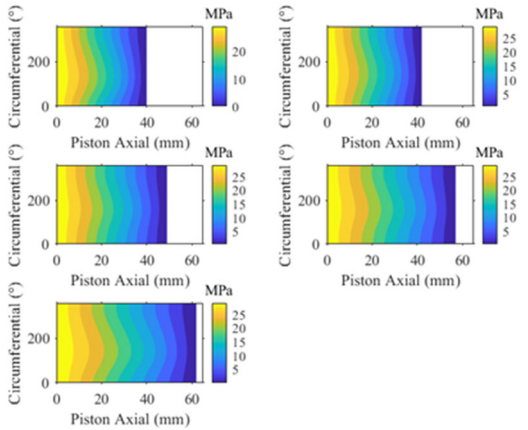

Figure 10 Pressure distribution in the high-pressure zone (t_0 = 0 μm)

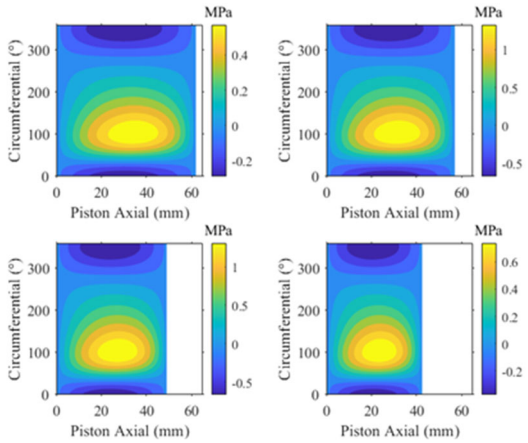

Figure 11 Pressure distribution in the low-pressure zone (t_0 = −1 μm)

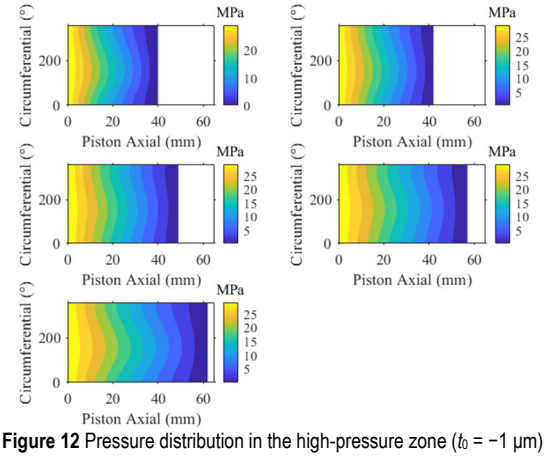

Figure 12 Pressure distribution in the high-pressure zone (t_0 = −1 μm)

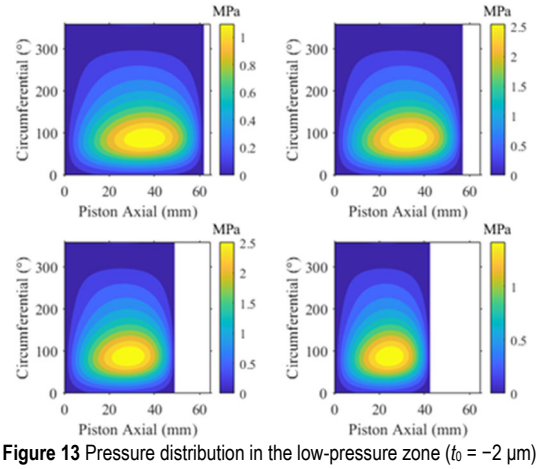

Figure 13 Pressure distribution in the low-pressure zone (t_0 = −2 μm)

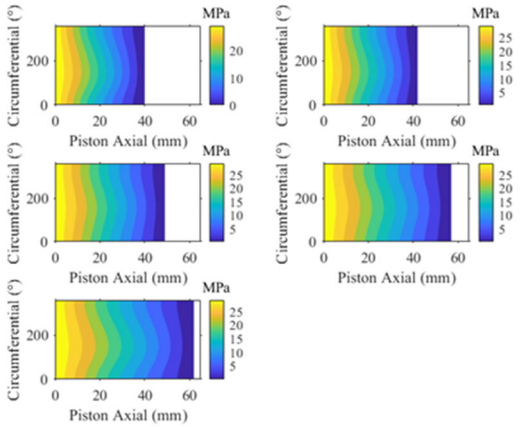

Figure 14 Pressure distribution in the high-pressure zone (t_0 = −2 μm)

Given the mean diametral clearance of 23 μm, the mean radial clearance is δ_m = 11.5 μm. For the reference case, the inlet radial clearance is δ = 11 μm and the outlet radial clearance is $\delta_2 = \delta + t_0$. The representative eccentricities used in the case study are e_1 = 1.1 μm, e_2 = −2.8 μm, e_3 = 2.0 μm and e_4 = −1.2 μm. These values lead to $e(0)$ = 3.0463 μm and $e(l)$ = 2.2825 μm for the baseline geometry.

Fig. 6, 8, 10, 12 and Fig. 14 show the pressure distributions at representative positions in the high-pressure zone (discharge zone) for different taper values. In all cases, the pressure decreases along the axial direction towards the outlet. For positive taper, the axial pressure drop becomes steeper as the taper magnitude increases; for negative taper, the opposite tendency is observed.

Fig. 5, 7, 9, 11 and Fig. 13 show the pressure distributions in the low-pressure zone (suction zone). For positive taper, where the inlet-outlet pressure difference is negligible, the flow is mainly driven by piston motion and the model predicts a local pressure decrease in the middle region. For the zero-taper case, the behaviour is similar but the low-pressure interval is narrower. For negative taper, the predicted low-pressure-zone pressure rises with taper magnitude. These negative values are gauge pressures from the analytical model; because no cavitation boundary is imposed, they indicate a tendency towards pressure depletion rather than physically sustainable absolute negative pressure.

Fig. 15 summarises the calculated location of the centre of pressure of the annular oil-film force in the discharge zone. The analytical model places this point close to the lower one-third of the sealing length measured from the piston bottom.

Fig. 16 shows the variation of the resultant hydraulic force acting on the piston with cylinder-block angle. The quantity plotted in Fig. 17 is a force, not a pressure. The resultant hydraulic force carried by the oil film is substantially larger in the discharge zone than in the suction zone, and its maximum value is about 2500 N near Bottom Dead Centre (BDC). Abrupt changes appear at the transitions between suction and discharge. The taper direction has only a limited influence on the magnitude of this resultant hydraulic force.

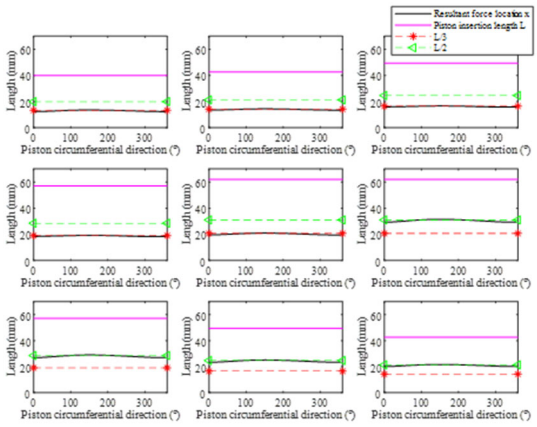

Figure 15 Location of the centre of pressure of the annular oil-film force on the piston

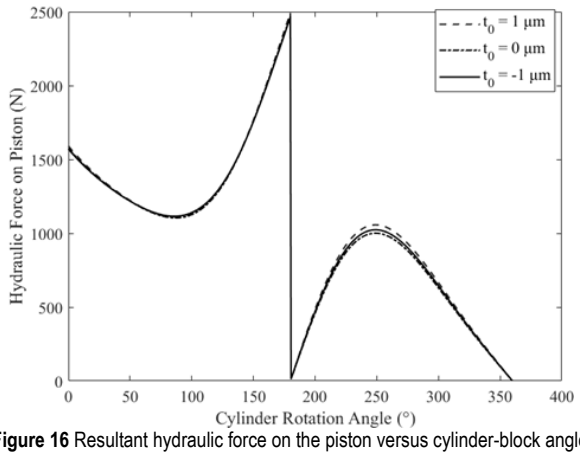

Figure 16 Resultant hydraulic force on the piston versus cylinder-block angle

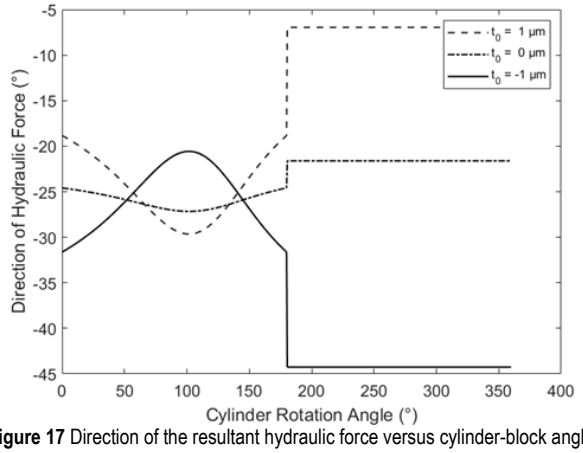

Figure 17 Direction of the resultant hydraulic force versus cylinder-block angle

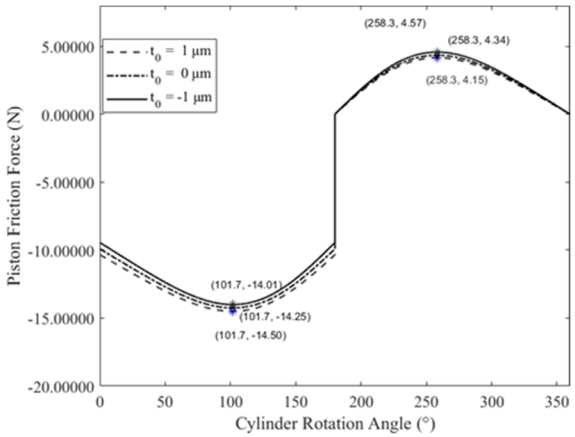

Figure 18 Variation of friction force with cylinder-block angle

Fig. 18 shows the corresponding variation of viscous friction force with cylinder-block angle. Because the oil film provides lubrication in the annular clearance, the calculated friction force is relatively small. The friction force is larger in the discharge zone than in the suction zone. In the discharge zone, a positive taper gives a larger friction force than a negative taper, while the zero-taper case lies in between; the trend is reversed in the suction zone.

The present Figures explicitly compare five taper magnitudes. In addition, Eq. (7), Eg. (24) and Eq. (39) to Eq. (42) indicate that the response is also sensitive to eccentricity, sliding speed, viscosity and clearance through $h(x, \theta)$, μ and u. For fixed geometry, higher viscosity or higher $|u|$ increases the viscous contribution, whereas clearance and eccentricity strongly affect the pressure gradient and load-carrying behaviour. A full multi-parameter numerical sensitivity map is beyond the scope of the present case study and is left for future work.

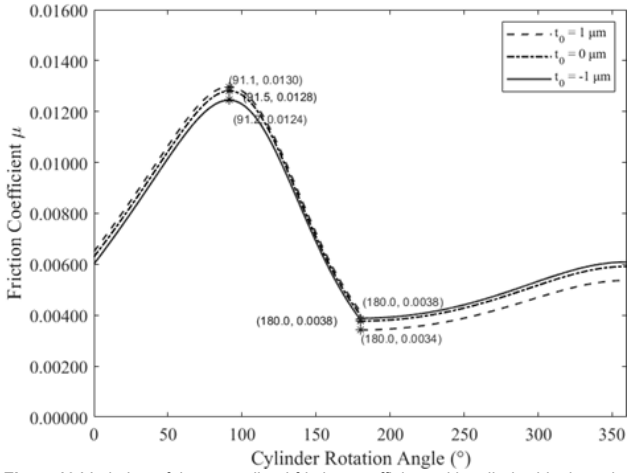

Figure19 Variation of the normalised friction coefficient with cylinder-block angle

Fig. 19 shows that the normalised friction coefficient varies with cylinder-block angle. In the present oil-film model, this quantity is used as a comparative friction indicator rather than direct proof of a boundary-lubrication regime. The results suggest more severe lubrication conditions at some angular positions, especially in the discharge zone, but rigorous regime classification would require roughness/contact modelling or an explicit mixed-lubrication criterion. The taper-direction trend is the same as that observed for the friction force.

4 CONCLUSION

This paper presents a numerical case study of a piston pair in a swash-plate axial piston pump. By including both machining taper and operational tilt, the revised manuscript focuses on the pressure distribution, resultant hydraulic force, centre of pressure and viscous friction in the piston-bore clearance.

(1) For the present CCY14-1B case, pressure decreases axially towards the outlet in the discharge zone. In the suction zone, the negative values predicted by the model are gauge pressures and indicate a tendency towards pressure depletion; they should not be interpreted as sustained absolute negative pressures.

(2) The resultant hydraulic force carried by the oil film is much larger in the discharge zone than in the suction zone and reaches its maximum near BDC. The taper direction has only a limited influence on the magnitude of this resultant force, whereas the centre of pressure in the discharge zone is located close to the lower one-third of the sealing length.

(3) The viscous friction force is relatively small under the full-film assumptions adopted here but is sensitive to taper direction. In the discharge zone, a positive taper yields higher friction than a negative taper; the trend is reversed in the suction zone. The reported friction coefficient should therefore be interpreted as a normalised friction indicator for the present oil-film model.

(4) The present paper does not yet include an independent experiment or CFD benchmark, so the conclusions should be regarded as case-specific analytical/numerical findings rather than universally validated laws. Future work will extend the study to broader parametric sensitivity and independent experimental validation.

5 REFERENCES

[1] Novaković, B., Radovanović, Lj., Đurđev, M., Đorđević, L., & Desnica, E. (2024). Analysis of the behaviour of the hydraulic fluid HM VG 32 and HV 32 at different operating conditions of the axial-piston pump. *Tehnički vjesnik*, *31*(5), 1523-1529. https://doi.org/10.17559/TV-20230524000667

[2] Zhao, Y., Feng, Z., Li, Y., Feng, L., Li, Q., & Cui, W. (2022). Analysis of contact surface wear performance of O-ring dynamic seal based on Archard model. *Tehnički vjesnik*, *29*(5), 1441-1453. https://doi.org/10.17559/TV-20210913080305

[3] Ouyang, X., Wang, T., & Fang, X. (2018). Research status of the high-speed aircraft piston pump. *Chinese Hydraulics & Pneumatics*, *42*(2), 1-8.

[4] Hidri, L. (2025). Solving Multi-stage Flexible Flow Shop Scheduling Problem with Cooling Times in the Steel Industry. *Studies in Informatics and Control*, *34*(1), 47-56. https://doi.org/10.24846/v34i1y202504

[5] Chen, X., Gao, W., & Ji, H. (2021). Leakage flow analysis for piston pair considering pose and taper. *Machine Tool & Hydraulics*, *49*(7), 14-21.

[6] Zheng, L., Li, G., Bai, S. et al. (2023). Analysis of lubrication characteristics of piston pair in large displacement axial piston pump. *Chinese Hydraulics & Pneumatics*, *47*(3), 17-27.

[7] Bergada, J. M., Kumar, S., Davies, D. Ll., & Watton, J. (2012). A complete analysis of axial piston pump leakage and output flow ripples. *Applied Mathematical Modelling, 36*(4), 1731-1751. https://doi.org/10.1016/j.apm.2011.09.016

[8] Kumar, S. & Bergadà, J. M. (2013). The effect of piston grooves performance in an axial piston pumps via CFD analysis. *International Journal of Mechanical Sciences*, *66*, 168-179. https://doi.org/10.1016/j.ijmecsci.2012.11.005

[9] Yang, L., Wang, L. Y., Li, L., Zheng, X. H., & Chang, S. Y. (2025). A Simulation-Based Optimization Approach to Enhance Drive Shaft Fatigue Strength. *International Journal of Simulation Modelling*, *24*(1), 123-134. https://doi.org/10.2507/IJSIMM24-1-CO1

[10] Xu, Y., Wang, R., Deng, M., Gu, Z., Xie, Y., & Jiao, Z. (2025). Flow Ripple Reduction of Axial Piston Pump for Multiple Working Statuses with Fast Structural Optimization Method. *Chinese Journal of Mechanical Engineering*, 38, 118. https://doi.org/10.1186/s10033-025-01252-4

[11] Du, Y., Cao, Q., Wang, W., Li, N., & Liu, X. (2023). Lubrication and leakage characteristics of piston pair in plunger pump considering elastic deformation. *Machine Tool & Hydraulics*, *51*(16), 144-149.

[12] Wang, K. (2020). *Micro-motion and lubrication characteristics of piston-cylinder interface in axial piston pump*. Harbin Institute of Technology, Harbin.
[13] Wang, K., Jiang, J., & Liu, Z. (2016). Axial piston pump piston cavity pressure and its effect on piston micro-motion. *Proceedings of the 9th National Conference on Fluid Power and Control*, 509-513.
[14] Mukherjee, S., Vacca, A., Shang, L., & Sharma, A. (2023). A thermal modeling approach for the piston/cylinder interface of an axial piston machine under asperity contact. *Meccanica*, *58*(10), 1929-1957. https://doi.org/10.1007/s11012-023-01709-7
[15] Lin, N., Wang, J., Wang, Q. et al. (2023). Progress on tribological characteristics and surface texturing of piston pairs in axial piston pump. *Journal of Taiyuan University of Technology*, *54*(4), 585-598.
[16] Haidak, G., Wei, X., Li, F., Larbi, A., & Wang, D. (2022). Heat effects modelling on the efficiency loss of the lubricating interface between piston and cylinder in axial piston pumps. *Tribology International*, *175*, 107846. https://doi.org/10.1016/j.triboint.2022.107846
[17] Lü, F., Xu, B., & Zhang, J. (2018). Simulative analysis of piston posture and piston cylinder interface leakage of EHA pumps by the influence of rotating speed. *Journal of Mechanical Engineering*, *54*(20), 123-130. https://doi.org/10.3901/JME.2018.20.123
[18] Liu, R., Zeng, Y., Hu, M., Zhu, C., Liu, C., & Wang, L. (2023). An investigation into the micro-geometric tapered-shape surface design of the piston bore of a piston-cylinder interface in an axial piston motor. *Mechanical Sciences*, *14*, 259-275. https://doi.org/10.5194/ms-14-259-2023
[19] Wang, X., Liu, Y., Zhang, J., & Chen, H. (2024). Tolerance design guideline for piston/cylinder interface of electro-hydrostatic actuator pumps based on a thermal-fluid-structure model. *Tribology International*, *191*, 109208. https://doi.org/10.1016/j.triboint.2023.109208
[20] Nie, S., Guo, M., Yin, F., Ji, H., Ma, Z., Hu, Z., & Zhou, X. (2021). Research on fluid-structure interaction for piston/cylinder tribopair of seawater hydraulic axial piston pump in deep-sea environment. *Ocean Engineering*, *219*, 108222. https://doi.org/10.1016/j.oceaneng.2020.108222
[21] Huang, W., Li, X., Wan, H., Lv, Y., Cai, J., & Yang, Y. (2025). Conical cylinder block: A key solution to alleviate cavitation in the piston chamber of axial piston pumps. *Physics of Fluids*, *37*(8), 086140. https://doi.org/10.1063/5.0279179
[22] Wang, W., Chao, Q., Shi, J., & Liu, C. (2025). Condition monitoring of axial piston pumps based on machine learning-driven real-time CFD simulation. *Engineering Applications of Computational Fluid Mechanics*, *19*(1), 2474676. https://doi.org/10.1080/19942060.2025.2474676
[23] Wang, Z., Chao, Q., Wang, W., Zhang, Z., & Liu, C. (2025). Transfer learning from computational fluid dynamics simulation data to experimental data for the fault diagnosis of axial piston pumps. *Engineering Applications of Artificial Intelligence*, *162*, 112643. https://doi.org/10.1016/j.engappai.2025.112643

Contact information:

Bin ZHANG
Taizhou Vocational and Technical College,
No. 8, Tianxing Road, Medical High-tech Zone, Taizhou City,
Jiangsu Province, China
E-mail: 396750516@qq.com

Shusheng LI
(Corresponding author)
Taizhou Vocational and Technical College,
No. 8, Tianxing Road, Medical High-tech Zone, Taizhou City,
Jiangsu Province, China
E-mail: 1162423185@qq.com

Wenke GAO
Shenzhen Technology University,
No. 3002, Lantian Road, Pingshan District, Shenzhen City,
Guangdong Province, China
E-mail: gaowenke@sztu.edu.cn